Int J Thermophys (2012) 33:2095–2102
DOI 10.1007/s10765-012-1292-z

Lock-in and Heterodyne Carrierographic Imaging Characterization of Industrial Multicrystalline Silicon Solar Cells

A. Melnikov · P. Chen · Y. Zhang · A. Mandelis

Published online: 10 October 2012

Abstract A novel non-destructive, non-contact laser-induced near-infrared imaging technique using an InGaAs camera and based on dynamic carrierography (a spectrally gated modulated photoluminescence modality) was used in direct lock-in (LICG) and heterodyne (HDCG) modes to characterize industrial multicrystalline silicon solar cells. The image amplitude depends on the free-photocarrier diffusion-wave density, the spatial resolution is a function of modulation frequency, and the contrast is due to the spatial distribution of important parameters influencing the efficiency of the solar cell, such as base recombination lifetime. High-spatial-resolution and high-frequency carrierographic images have been obtained using a HDCG method. The relationship between the LICG amplitude and the solar cell terminal photovoltage under an external load was investigated. The influence of surface recombination velocities and damage of the solar cell *p–n* junction was studied. A correlation between the solar cell efficiency and the surface-integrated LICG amplitude from the entire solar cell is presented.

Keywords Efficiency · Heterodyne carrierographic imaging · Lock-in carrierographic imaging · Silicon solar cell · Spatial distribution · Transport parameters

1 Introduction

Imaging techniques based on quasi-steady-state (dc) electroluminescence and photoluminescence (PL) are widely used for qualitative and quantitative characterization of silicon solar cells [1–6]. These types of imaging are extremely relevant for an

A. Melnikov · P. Chen · Y. Zhang · A. Mandelis (✉)
Center for Advanced Diffusion-Wave Technologies, Department of Mechanical and Industrial Engineering, University of Toronto, 5 King's College Rd., Toronto, ON M5S 3G8, Canada
e-mail: mandelis@mie.utoronto.ca

estimation of the efficiency of solar cells using non-contacting methods [7,8]. Laser photocarrier radiometry (PCR) of semiconductors [9] is a form of modulated PL, spectrally gated to filter out thermal infrared spectral contributions. It is sensitive to diffusive photocarrier-wave transport properties and band-to-defect recombination with signals linear or supralinear in the excess photocarrier density. PCR can be used for depth controlled imaging characterization of solar cells. It has been shown that the PCR signal is very sensitive not only to photocarrier-wave transport properties but also to external load in solar cells [10]. Lock-in carrierography (LICG), the dynamic imaging extension of PCR, was recently introduced using a spread superband-gap laser beam and a near-infrared (NIR) InGaAs camera [11]. In the first reported embodiment of this technique, only low modulation frequencies ($\leq$10 Hz) could be used in order to maximize the image signal-to-noise ratio through oversampling. However, LICG of Si-based devices can yield much needed improved spatial (radial and axial) resolution of optoelectronic defects at shallow depths below the illuminated surface only at frequencies much higher than today's state-of-the-art InGaAs camera capabilities, as required by the depth probing ac carrier diffusion length. To overcome this restriction, the heterodyne scheme is introduced to achieve high-frequency CG imaging through use of carrier-wave superposition beats. In addition, the effects of the load resistance, shunt resistance, and surface recombination velocity on CG imaging were investigated. The correlation between the surface-integrated LICG amplitude and its empirical relationship to solar efficiency is identified. Correlations for photovoltage and solar cell efficiency are presented.

2 Experimental Setup and Specimens

A schematic of the experimental setup for CG imaging is shown in Fig. 1. The system consists of a high-speed NIR InGaAs snapshot camera with windowing, two fiber coupled 808 nm, 9 W diode lasers, optical blocks with collimator and diffuser, a two-channel function generator, a data acquisition module, and a frame grabber. A long-pass filter LP-1000 nm is used to prevent the excitation laser beams from interfering with the NIR camera. An optical block with a microlens array diffuser

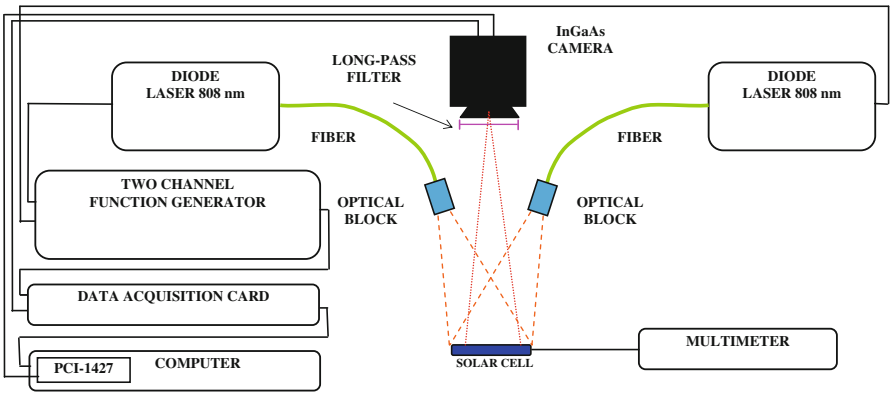

Fig. 1 Experimental setup for direct and heterodyne lock-in carrierographic imaging

was used for each laser beam to avoid inhomogeneous solar cell illumination. Both lasers were modulated sinusoidally in parallel at the same frequency for direct lock-in imaging. The data acquisition module USB 6259 is used to generate sinusoidal modulation and reference signals from one of its analog outputs and the trigger signal of the infrared camera from its digital I/O. Synchronous undersampling with external triggering of the camera was implemented for lock-in in-phase (IP) and quadrature (Q) images to produce computer-generated amplitude and phase images. Sixteen images per correlation period were scanned with a maximal camera exposure time of 16 ms per image. For heterodyne lock-in imaging, the two lasers were sinusoidally modulated with a frequency of 5 kHz for the first laser and 5.01 kHz for the second laser, using a two-channel function generator. The 10 Hz reference signal (same as before) and the trigger signal were produced by the data acquisition card. For synchronization of all signals, modulation was started at the first sampling instant and was stopped after each correlation period. Amplitude and phase images were obtained from IP and Q images at the beat frequency $\Delta f = 10$ Hz in the same manner as with direct lock-in imaging, and with the maximum NIR camera exposure time of 16.6 ms.

An industrial multicrystalline (mc) silicon solar cell (156×156 mm^2 area, 200 μm thickness, p-type base, from Enfoton, Cyprus) was used for measurements. The external load resistance was used for changing the voltage across the p–n junction. To change the surface recombination and simulate p–n junction damage, the solar cell was gently rubbed with fine sand paper once or several times. The direction of the rubbing was along the grid lines to prevent their destruction leading to a significant series resistance increase of damaged areas.

3 Results

A typical LICG amplitude image of an mc-Si solar cell at low-frequency modulation is shown in Fig. 2a. The image shows high inhomogeneity of the free photo-carriers diffusion-wave density distribution recombination, leading to the CG image over the cell. The carrier diffusion-wave density (and thus imaging spatial contrast) depends on solar cell transport parameters, mainly, the base recombination lifetime, front- and

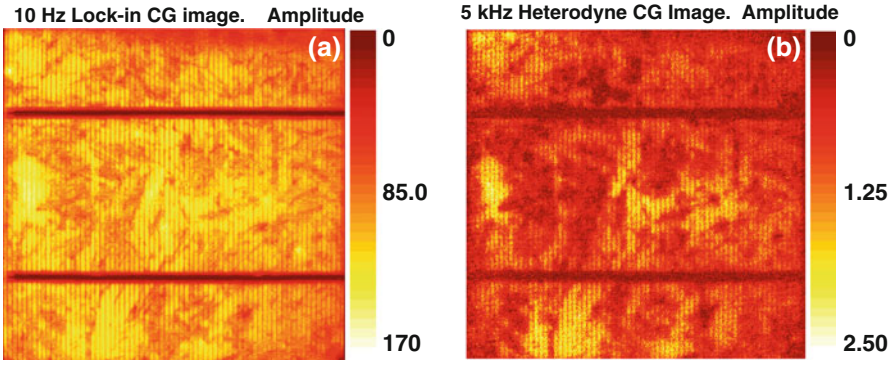

Fig. 2 (a) Direct 10 Hz lock-in amplitude and (b) 5 kHz heterodyne lock-in amplitude CG images of a typical mc-Si solar cell, obtained using an InGaAs camera with 16 ms exposure time

back-surface recombination velocities, and the emitter and base minority carrier diffusion coefficient, as well as the p–n junction voltage [9,12]. The spatial resolution of these parameters is limited due to the diffusive character of recombination which is controlled by the ac carrier diffusion length,

$$L_e(\omega) = \sqrt{(D^*\tau)/(1 + i\omega\tau)}, \tag{1}$$

where D^* is the ambipolar carrier diffusivity, τ is the minority recombination lifetime, and ω is the angular modulation frequency. For typical mc-Si lifetimes (1 μs to 100 μs), the ac minority carrier diffusion length at 10 Hz practically coincides with the dc diffusion length. As a result, LICG images exhibit the same resolution as dc PL images. However, LICG produces phase images as a second independent imaging channel, while the dark current in the camera pixels as well as the noise and dc background are strongly suppressed in the lock-in method. According to Eq. 1, the spatial resolution increases with the increasing modulation frequency to the kHz range. This is tantamount to a carrier density wavelength decrease. It has been shown in spot-by-spot PCR images of mc-solar cells [13] that contrast and spatial resolution improve greatly at high frequencies. However, for camera-based imaging, high-frequency demands decrease with the exposure time, resulting in significant signal quality deterioration. To overcome this problem, we introduced heterodyne lock-in CG imaging. The 5 kHz heterodyne carrierography (HDCG) image equivalent of Fig. 2a is presented in Fig. 2b. This image exhibits higher resolution and contrast compared to the direct 10 Hz LICG image. Because of the shorter ac diffusion length, the high-frequency carrier-wave density depth distribution samples regions closer to the surface, and the image is dominated by near-surface defects affecting the junction-area photovoltaic energy conversion. The HDCG amplitude depends on the same transport parameters as the LICG amplitude, but the existence of HDCG images hinges on the nonlinearity of the PCR (modulated PL) response [14]. The sources of PCR nonlinearity are the dependence of transport parameters on the level of injection, the band-to-band and/or band-to-defect recombination mechanisms, and the modulation of the p–n junction energy barrier [12]. The nonlinearity of CG signals leads to an additional enhancement of HDCG image contrast.

The dependence of the surface-integrated LICG amplitude on the p–n junction voltage under constant laser beam intensity is presented in Fig. 3. The inhomogeneity of transport parameters is clearly visible in the statistical distribution of the GC image pixel amplitude (inset of Fig. 3a, b). This distribution shows the fraction of area with high, middle, and low lifetimes, as well as the sum of areas which do not generate a photocurrent (area under the contact electrode, under the grid, and the missing upper left corner of cell). The dependence of the surface-integrated LICG amplitude on the terminal photovoltage exhibits an exponential behavior under 10 Hz laser illumination. This is broadly explained by the fact that under dc conditions the photovoltage is related to the excess minority carrier in the form [15],

$$eU = \Delta\eta \approx kT \ln\left(\frac{\Delta n(\Delta n + N_D)}{n_i^2}\right) \approx kT \ln(I_{PL}) + C, \tag{2}$$

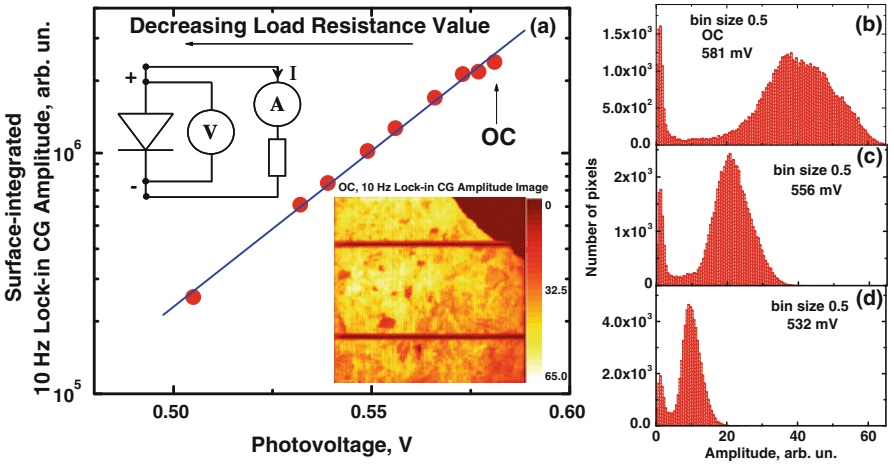

Fig. 3 (a) Surface-integrated 10 Hz LICG amplitude dependence on terminal photovoltage and statistical distribution of pixel amplitudes for photovoltage of (b) 592 mV, (c) 556 mV, and (d) 532 mV. Laser power is ∼15 W. Photovoltage was changed as a function of load resistance and was measured at maximum laser power

where η is the separation of quasi-Fermi energies, N_D is the doping concentration, Δn is the excess minority carrier concentration, and I_{PL} is dc PL intensity. Here η is assumed constant along the base width. Although for our case the depth distribution of the minority carrier in the base is not constant at 808 nm laser illumination, a similar logarithmic dependence of the surface-integrated CG signal on the photovoltage is observed. A detailed theoretical explanation of this fact has been developed in [16]. The statistical distribution peak shifts toward low radiative amplitudes with decreasing photovoltage under a smaller load resistance, Fig. 3a–d. The statistical distribution shows the number of pixels with amplitude values within the range of x and $x + \Delta x$, where Δx is the "bin size." At the same time, there is also a reduction of the full width half maximum (FWHM). It should be mentioned that because of the surface metallic grid, the local photovoltage can be assumed constant over the surface of the investigated solar cell under a small illumination intensity ($0.04\,\mathrm{W}\cdot\mathrm{cm}^{-2}$). The presence of the grid minimizes or eliminates areas of high series resistance and leads to an outflow of excess minority carriers from areas with a high carrier lifetime to areas with a low carrier lifetime as well as to a shunt resistance under open circuit conditions. As a result, PL from areas with a long carrier lifetime significantly decreases and the surface-integrated CG amplitude reflects the terminal voltage as well as average transport parameters that determine the generation current across the entire solar cell. It should be mentioned that areas with a high series resistance can be easily observed using LICG amplitude imaging as high-amplitude regions.

For a more detailed investigation of the influence of transport parameters on LICG images, sequential rubbing with fine sandpaper was performed. The 10 Hz LICG amplitude images under an open circuit (OC) condition and the related pixel amplitude statistical distributions are shown in Fig. 4. The surface mechanical damage causes a significant increase of the surface recombination velocity as well as damage of the p–n

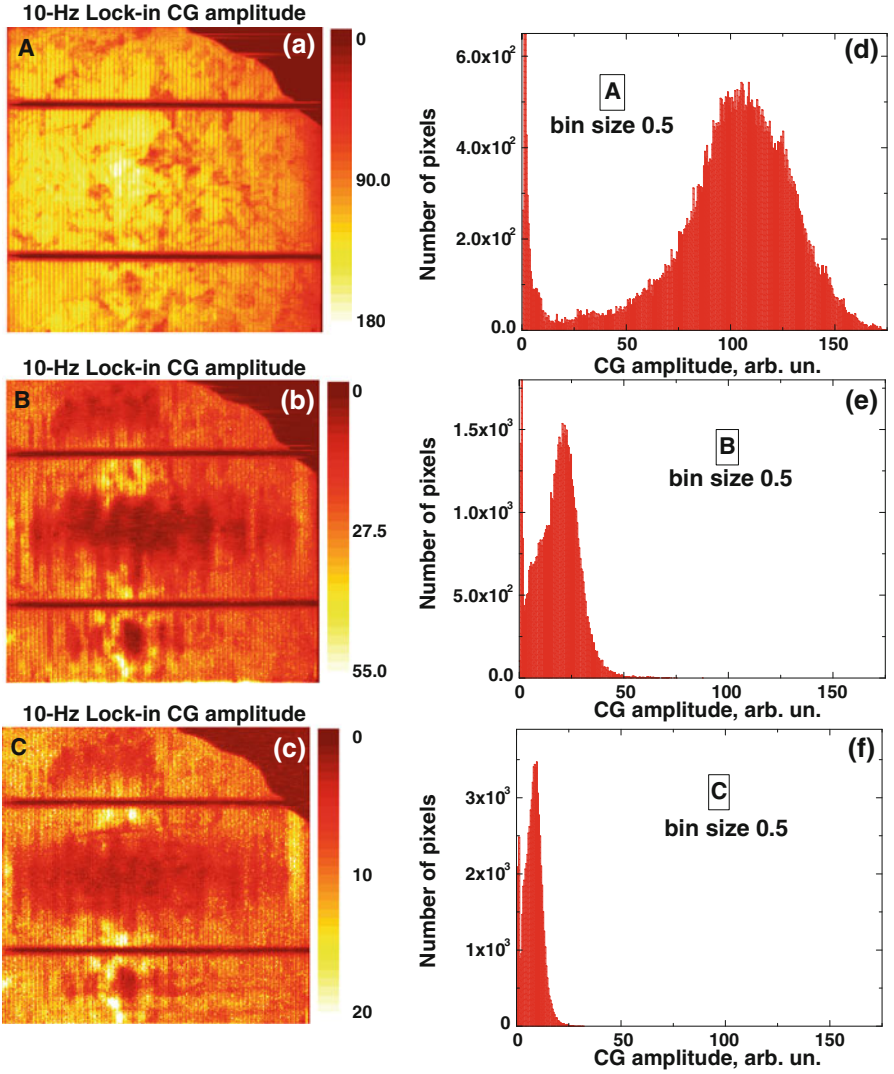

Fig. 4 Direct 10 Hz lock-in amplitude CG images of mc-Si solar cell (a) before and (b,c) after sequential rubbing with fine sand paper, and (d–f) the corresponding statistical distributions of pixel CG amplitudes

junction and the appearance of decreasing local shunt resistances. In the images, the damage areas can be clearly seen as areas of a significantly decreased LICG amplitude. Interestingly, the LICG amplitude of undamaged areas decreases, too. In a manner similar to the influence of the load resistance on the statistical pixel amplitude distribution, the peak of the latter shifts toward that corresponding to null radiative emission areas, accompanied by a distribution FWHM decrease. The decrease of the LICG amplitude of the undamaged areas confirms the effective outflow of excess minority carriers from the undamaged into the damaged areas. As the I–V characteristics show, Fig. 5a, the

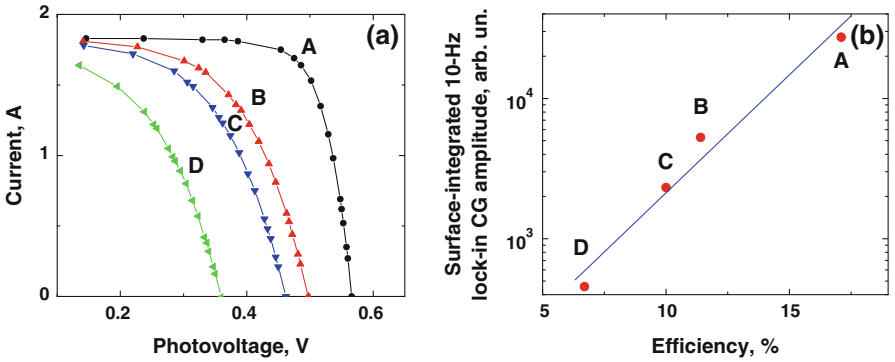

Fig. 5 (a) Current–voltage characteristics of the mc-Si solar cell of Fig. 4 before and after sequential rubbing with sand paper, under 0.021 W · cm^{-2}, 808 nm laser beam illumination, obtained through change of load resistance, and (b) correlation between solar efficiency and surface-integrated 10 Hz CG lock-in amplitude. *D* indicates the case of full surface damage

surface damage leads to a small decrease in the short-circuit current and a higher decrease in the OC photovoltage. This is consistent with the appearance of finite local shunt resistances as well as decreases of effective base lifetimes due to an enhanced surface recombination velocity. It also leads to a significant decrease of the solar-cell efficiency. The dependence of the surface-integrated lock-in CG amplitude on solar efficiency as calculated from the *I–V* characteristics is shown in Fig. 5b. The solar efficiency is approximately proportional to the logarithm of the surface-integrated LICG amplitude, in agreement with theory [16].

4 Conclusions

Direct lock-in and heterodyne carrierographic imaging were introduced, and solar cell applications were demonstrated. High-frequency HDCG exhibits significant higher spatial resolution and inhomogeneity contrast of mc-Si solar cells compared with low-frequency direct LICG imaging. The CG amplitude depends on transport parameters, mainly the carrier lifetime, and surface recombination velocities, as well as the terminal photovoltage. The surface-integrated CG amplitude depends exponentially on the terminal photovoltage. The surface-integrated LICG amplitude can be used for estimation of the electrical parameters and the dollar efficiency of mc-Si solar cells.

Acknowledgments A. Mandelis gratefully acknowledges the support of the Canada Foundation for Innovation (CFI) and the Ontario Research Fund (ORF), the Natural Sciences and Engineering Research Council of Canada (NSERC) for a Discovery Grant, the Canada Research Chairs (CRC) program, and USRA awards to P. Chen.

References

1. T. Fuyuki, H. Kondo, T. Yamazaki, Y. Takahashi, Y. Uraoka, Appl. Phys. Lett. **86**, 262108 (2005)
2. P. Würfel, T. Trupke, T. Puzzer, E. Schäffer, W. Warta, S.W. Glunz, J. Appl. Phys. **101**, 123110 (2007)

3. T. Trupke, R.A. Bardos, M.D. Abbott, Appl. Phys. Lett. **87**, 184102 (2005)
4. J.A. Gisecke, M.C. Schubert, B. Michl, F. Shubert, W. Warta, Sol. Energy Mater. Sol. Cells **95**, 1011 (2011)
5. T. Trupke, E. Pink, R.A. Bardos, M.D. Abbott, Appl. Phys. Lett. **90**, 093506 (2007)
6. M. Kasemann, D. Grote, B. Walter, W. Kwapil, T. Trupke, Y. Augarten, R.A. Bardos, E. Pink, M.D. Abbott, W. Warta, Prog. Photovoltaics Res. Appl. **16**, 297 (2008)
7. I. Latchford, J.B. True, Photovoltaics World **2011**, Iss. 4 (2011)
8. B. Michl, M. Rüdiger, J.A. Giesecke, M. Hermle, W. Warta, M.C. Schubert, Sol. Energy Mater. Sol. Cells **98**, 441 (2012)
9. A. Mandelis, J. Batista, D. Shaughnessy, Phys. Rev. B **67**, 205208 (2003)
10. A. Melnikov, A. Mandelis, J. Tolev, E. Lioudakis, J. Phys. Confer. Ser. **214**, 012111 (2010)
11. A. Melnikov, A. Mandelis, J. Tolev, P. Chen, S. Huq, J. Appl. Phys. **107**, 114513 (2010)
12. A. Mandelis, J. Appl. Phys. **66**, 5572 (1989)
13. A. Mandelis, A. Melnikov, J. Tolev, J. Xia, S. Huq, E. Lioudakis, Quant. InfraRed Thermogr. J. **7**, 35 (2010)
14. J. Tolev, A. Mandelis, M. Pawlak, J. Electrochem. Soc. **154**, H983 (2007)
15. T. Trupke, R.A. Bardos, M.D. Abbott, J.E. Gotter, Appl. Phys. Lett. **87**, 093503 (2005)
16. A. Mandelis, Y. Zhang, A. Melnikov, J. Appl. Phys. **112**, 054505 (2012)